Active flow control of the airflow of a ship at yaw

Ocean Engineering 273 (2023) 113961

Contents lists available at ScienceDirect

Ocean Engineering

journal homepage: www.elsevier.com/locate/oceaneng

Active flow control of the airflow of a ship at yaw

Kewei Xu *, Xinchao Su, Yutao Xia, Yitong Wu, Rickard Bensow, Sinisa Krajnovic

Department of Mechanics and Maritime Sciences, Chalmers University of Technology, Gothenburg, 412 96, Sweden

ARTICLE INFO

Keywords:
Active flow control (AFC)
Wake flow
Yaw effect
Large eddy simulation (LES)
Experiments

ABSTRACT

This paper implements the steady Coanda effect active flow control (AFC) on the Chalmers ship model (CSM) to study its influence on the ship's side force and airwake under the yaw effect. The study is conducted numerically using Large Eddy Simulation (LES) with Wall-Adapting Local-Eddy Viscosity (WALE) model. Numerical methods are validated by the experimental data acquired from the baseline CSM under 10° port-side wind. The model with AFC is created by modifying the square-shaped hanger base to the Coanda surface and added with injection slots along the base's roof edge and two side edges. The results show that the base-shape modification significantly alters the vortex structure on deck from z-direction vortex (ZV) to streamwise vortex (SV), and the steady Coanda effect with a momentum coefficient (C_μ) of 0.02 further enhances the SV with the removal of port-side vortex (PV). The side force and yaw moment are reduced by 5.27% and 7.97%, respectively in the AFC case due to the reduction of port-side (windward) ship-surface pressure. Furthermore, the current AFC can suppress the low-speed region and alleviate the velocity gradient in the lateral direction, which mitigates the regions of high TKE (turbulent kinetic energy) and high shear stress along the port-side deck.

1. Introduction

Extensive studies have been conducted on the ship's air wake (Syms, 2008; Forrest and Owen, 2010; Herry et al., 2011; Kääriä et al., 2013; Gallas et al., 2017; Crozon et al., 2018; Shukla et al., 2021; Nisham et al., 2021) that is characterized by large unsteadiness, massive separation, and shear layer interactions. Under the yaw effect (cross-flow or wind-on-deck, WOD), the flow structure becomes even more complex (Rhoades and Healey, 1992; Zan, 2001) with enhanced unsteadiness. The ship's air wake, therefore, poses a serious challenge for helicopter recovery and launch, leading to significantly increased pilot's workload and safety issues (Forrest and Owen, 2010). A yaw effect also has negative influences on side forces, which reduces ships' stability and maneuverability. In this regard, flow control is expected to play a critical role in countering the above influences under the yaw effect.

Flow control can be categorized as passive flow control (PFC) that does not require external flow source, and active flow control (AFC) that does. Significant efforts to suppress the influence of yaw is made from the passive flow control perspective. Greenwell and Barrett (2006) experimentally tested the inclined screen flow-control structures with various inclined angles, blockages, and locations on the Simplified Frigate Shape (SFS). With a 30° cross-flow, it was found that the tested configurations have limited effect on mitigating downwash flow but can substantially lower turbulence levels. Various fence structures were tested on the DDG-81 model by Findlay and Ghee (2006) to study their effectiveness in altering mean and fluctuating velocity in the vicinity of the deck region. The parameters of interest included type (solid or porous), angle, size, and location of the fence. It was suggested that the addition of the fence can improve the flow condition on deck by suppressing the mean momentum loss and turbulent intensity. However, these improvements became less significant under the yaw effect as the ship's air wake deviates from the flight deck. LaSalle (2013) placed a notched fence on the top and side of the hanger to modify ship airwake flow structures for more expansive helicopter flight envelopes. However, with 15° yaw, the fence structure was only capable of altering the shape and size of the re-circulation region but had a negligible effect on the turbulent kinetic energy and Reynolds shear stress. Various PFC techniques, including flap, ramp, and notch, were studied on a ship model in oblique wind-on-deck (WOD) conditions (Kaaria, 2012). The hanger notch configuration could reduce the RMS (root-mean-square) heave, pitch, and roll of landing helicopters by as much as 40%–45% during lateral translation and 30%–40% over the landing region. Similar studies were also conducted by Yongjie et al. (2019) who implemented ramp and notch on the side of a simplified LPD-17 ship model, and a remarkable reduction of RMS rotor moment was achieved by a side ramp in 15° WOD. Bardera et al. (2021) modified the hanger to a similar shape with the re-circulation bubble for an aerodynamically

* Corresponding author.
E-mail address: kewei@chalmers.se (K. Xu).

https://doi.org/10.1016/j.oceaneng.2023.113961
Received 15 November 2022; Received in revised form 25 January 2023; Accepted 12 February 2023
Available online 17 February 2023

optimized geometry. The angled and elliptical hangers with roof and sides modified achieved the overall best performance considering the mitigation of unsteadiness, reduction of low-speed area, and loss of interior volume. The study found that the geometrical modifications of roof and side were particularly effective to suppress the low-velocity areas behind the hanger in a broad range of WOD.

For the active flow control, Shafer and Ghee (2005) applied steady injection on the hanger base of a scaled DDG-81 ship model. Quantified by the velocity standard deviation, the unsteadiness in the landing region at zero yaw angle was reduced by 6.6% with the injection velocity of 2.5% of the free-stream. As the yaw angle increased to 20°, the reduction of unsteadiness was increased to 8.3% with the same injection velocity.

Overall, the previous flow control studies on ships at a yaw mainly focus on the suppression of unsteadiness, recovery of flow momentum loss, and improvement of helicopter operations. However, little attention has been paid to studying the flow control's effect on side force, which is critical for a ship's stability and maneuverability under the yaw effect. Moreover, most of the previous studies utilize passive flow control methods, whereas limited efforts have been made using active flow control that is more flexible with a higher potential in control effectiveness. Recently, Xu et al. (2022) implemented the steady Coanda effect AFC at the hanger-roof edge of the Chalmers ship model (CSM) and achieved desirable control effectiveness, including drag reduction and turbulent suppression in high energy efficiency. The study was conducted under the zero-yaw effect.

The present work is extended from the previous study (Xu et al., 2022) by considering the yaw effect and by applying the steady Coanda effect not only on the hanger-roof but also along both side-edges (details will be shown in Section 2). The objectives are to study the influences of this AFC on the side force for improving the ship's maneuverability and its influences on the mean and fluctuating quantities in the wake flow for benefiting maritime helicopter operation. The current study is conducted numerically using Large Eddy Simulation (LES) with Wall-Adapting Local-Eddy Viscosity (WALE) subgrid model. Experimental testing is also conducted to validate the numerical methods. Apart from studying the control effectiveness of the steady Coanda effect, the mechanism of turbulent suppression is also understood via the current study. To the authors' knowledge, the steady Coanda AFC has not been studied on ships for controlling airflow under the yaw effect. The present work is to shed some light on this topic.

The remainder of the paper is organized as follows: Section 2 introduces the experimental setup, including wind tunnel facilities, test equipment, and test conditions; it also describes the numerical setup, including numerical methods, boundary conditions, and mesh resolutions. Section 3 starts with baseline validations followed by flow control results including the reduction of side force and yaw moment as well as the suppression of turbulent kinetic energy (TKE) and shear stress with the discussion of the suppression mechanism. Section 4 discusses three issues of applying the current AFC to a real ship.

2. Description of work

2.1. Experimental setup

This section describes the details of experiments with the ship model placed at the 10° yaw angle. The side force (F_y), drag force (F_d), and the distribution of pressure coefficients of the baseline Chalmers ship model (CSM) are measured experimentally, which are later used to validate the numerical methods. The present experimental setup is adopted from our previous work at zero-yaw condition (Xu et al., 2022).

The baseline CSM as shown on the top of Fig. 1 is used in the present study that consists of a bow, hanger, base, deck, and stern. The width-to-height ratio (W/h) of the hanger is 0.45 and is similar to that of the simplified ship model (SFS2 Bardera and Meseguer, 2015). Details

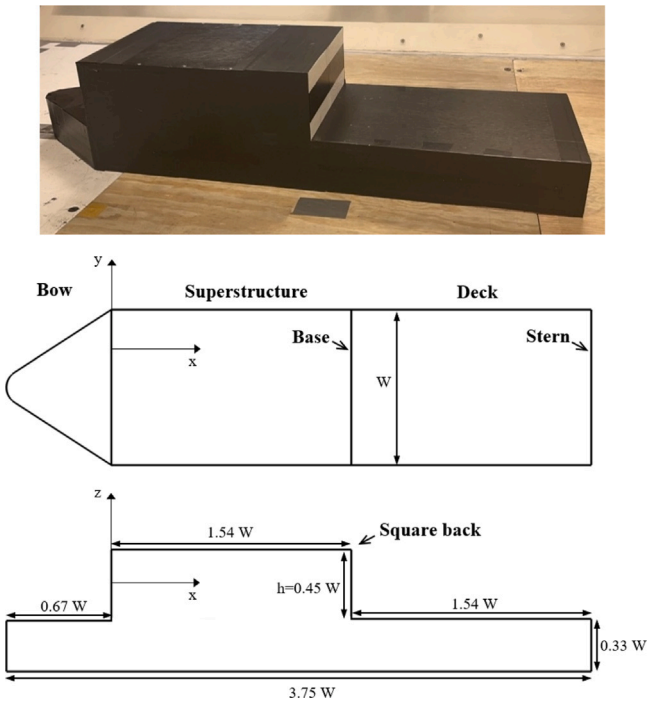

Fig. 1. The Chalmers ship model and its dimensions in top and side views.

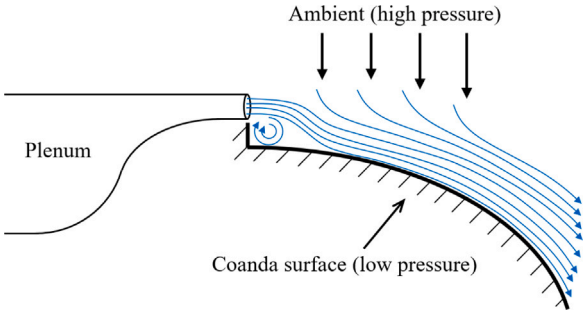

Fig. 2. Illustration of the Coanda effect (Xu et al., 2022).

of model dimensions are shown in the middle and bottom of Fig. 1. The width of the hanger (W) is used as the characteristic length for normalization.

The Coanda effect is illustrated by the sketch in Fig. 2, which is the tendency of a fluid jet to stay attached to a convex surface (Tritton, 2012). It is widely used for the active flow control on bluff bodies (Freund and Mungal, 1994; Barros et al., 2016; Haffner et al., 2020), ground vehicles (Geropp and Odenthal, 2000; Kee et al., 2001), and airfoils (Jones et al., 2002; Sellars et al., 2002; Jones, 2005; Seele et al., 2013).

The current flow control model shown in Fig. 3 is modified based on the baseline CSM, which adds the injection slots near all edges (two sides and roof) of the base and modifies the square-back to a quarter-ellipse-shape Coanda surface. The ellipse shape is kept the same among sides and roof with a semi-major axis (a) of 20%h and a semi-minor axis (b) of 15%h, where h is the hanger height. The ellipse shape is selected over a circular shape due to a higher radius of curvature that has a better attachment and stronger Coanda effect of the jet flow. The ellipse shape and jet slot size are adopted from our previous study (Xu et al., 2022). The modified ship base, therefore, consists of three regions as shown in Fig. 3: roof Coanda surface (green), sides

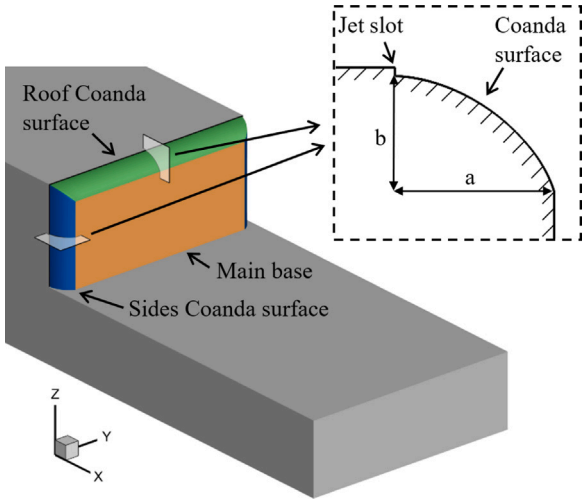

Fig. 3. Modification of Coanda surfaces and jet slots.

Table 1
Locations of pressure probes (x/W).

Numbers	1	2	3	4	5	6	7	8	9
Locations	0.08	0.14	0.24	0.54	0.73	0.92	1.10	1.25	1.38

Coanda surfaces (blue), and main base (orange). Modifying the square-back to the ellipse shape causes a volume loss of hanger by 0.4%.

The experiments on the baseline CSM are conducted in the closed-circuit L2 wind tunnel facilities at the Chalmers University of Technology as shown in Fig. 4. The closed test section of the wind tunnel has a cross-section of 1.8 m × 1.25 m with a length of 3 m. The blockage ratio of the baseline CSM in the test section is about 2.4%. The speed range of the wind tunnel is 0–60 m/s. The free-stream dynamic pressure and velocity are measured by the pitot tube placed at the beginning of the test section as shown in Fig. 4(a) and (c). The baseline CSM is tested at 5 m/s, which yields a Reynolds number (Re) of 8×10^4 based on the ship width. As illustrated in Fig. 4(a), the ship model is mounted on a six-component strain-gauge balance from RUAG of type 196-6H that is positioned underneath the tunnel floor. During testing, the ship model is exposed to a 10° port-side wind. This is achieved by rotating the force balance together with the ship model to the starboard (opposite) side as shown in Fig. 4(c). The side force (F_y) and drag force (F_d) acquired by the force balance is an averaged value for 20 s. The side force (C_y) and drag coefficient (C_d) are the normalization of F_y and F_d using Eqs. (1) and (2), respectively.

$$C_d = \frac{F_d}{0.5\rho_\infty {u_\infty}^2 A_s} \tag{1}$$

$$C_y = \frac{F_y}{0.5\rho_\infty {u_\infty}^2 A_s} \tag{2}$$

where ρ_∞ and u_∞ are the free-stream density and velocity, A_s is the ship cross sectional area at the zero-yaw position.

The pressure measurements are conducted using the differential pressure scanner 9116 with a scanning frequency of 62.5 Hz and a sampling time of 120 s. The pressure scanner is connected to the pressure probes using one-meter-long PVC tubes. The pressure distribution is obtained by the pressure probes located along the center of the deck as shown in Fig. 4(b). Table 1 presents the specific positions of probes relative to the base.

The pressure coefficient is obtained based on the measured pressure,

$$C_p = \frac{p - p_\infty}{0.5\rho_\infty {u_\infty}^2} \tag{3}$$

where p is the measured deck pressure, p_∞ is the free-stream pressure.

2.2. Numerical setup

This section describes the numerical setup of the present study. Large Eddy Simulation (LES) is conducted using the commercial finite volume software, Star-CCM+. The governing equations are the incompressible, spatially filtered 3D Navier–Stokes equations as shown in Eq. (4)–(6). The filter width, Δ, is associated with the cell size and is defined as $\Delta = (\Delta_i \Delta_j \Delta_k)^{1/3}$.

$$\nabla \cdot (\rho \tilde{\mathbf{v}}) = 0 \tag{4}$$

$$\frac{\partial}{\partial t}(\rho \tilde{\mathbf{v}}) + \nabla \cdot (\rho \tilde{\mathbf{v}} \otimes \tilde{\mathbf{v}}) = -\nabla \cdot \tilde{p}\mathbf{I} + \nabla \cdot (\tilde{\mathbf{T}} + \mathbf{T}_{SGS}) + \mathbf{f}_b \tag{5}$$

$$\frac{\partial}{\partial t}(\rho \tilde{E}) + \nabla \cdot (\rho \tilde{E} \tilde{\mathbf{v}}) = -\nabla \cdot \tilde{p}\tilde{\mathbf{v}} + \nabla \cdot (\tilde{\mathbf{T}} + \mathbf{T}_{SGS})\tilde{\mathbf{v}} - \nabla \cdot \tilde{\mathbf{q}} + \mathbf{f}_b \tilde{\mathbf{v}} \tag{6}$$

where ρ is the constant density, $\tilde{\mathbf{v}}$ is the filtered velocity, $\tilde{p}$ is the filtered pressure, $\mathbf{I}$ is the identity tensor, $\tilde{\mathbf{T}}$ is the filtered stress tensor, $\mathbf{f}_b$ is the resultant of the body forces, $\tilde{E}$ is the filtered total energy, and $\tilde{\mathbf{q}}$ is the filtered heat flux.

The subgrid scale stress tensor $\mathbf{T}_{SGS}$ is given in Eq. (7),

$$\mathbf{T}_{SGS} = 2\mu_t \tilde{\mathbf{S}} - \frac{2}{3}(\mu_t \nabla \cdot \tilde{\mathbf{v}})\mathbf{I} \tag{7}$$

where $\tilde{\mathbf{S}}$ is the strain rate tensor and μ_t is the subgrid scale viscosity.

The Wall-Adapting Local-Eddy Viscosity (WALE) model proposed by Nicoud and Ducros (1999) is employed in the present study to provide the subgrid scale viscosity (μ_t) in the Boussinesq approximation of the subgrid-scale stress tensor. The WALE model has been validated in our previous numerical study on the same ship model (Xu et al., 2022, 2023). It is also extensively validated on predicting flows around the hatch back (Aljure et al., 2014) and the square back (Dalla Longa et al., 2019) Ahmed bodies that represent the bluff-body shape of the current ship model. The WALE model is, therefore, suitable for the current numerical study.

The WALE model computes the subgrid eddy viscosity based on the invariants of the velocity gradient and accounts for rotational rate. It is defined as

$$\mu_t = \rho(C_w \Delta)^2 \frac{(S_{ij}^* S_{ij}^*)^{3/2}}{(\tilde{S}_{ij}\tilde{S}_{ij})^{5/2} + (S_{ij}^* S_{ij}^*)^{5/4}} \tag{8}$$

where the model coefficient C_w is 0.544. $\tilde{S}$ is the strain rate tensor computed from the resolved velocity field. S_{ij}^* is the traceless symmetric part of the square of the velocity gradient tensor, defined as

$$S_{ij}^* = \frac{1}{2}(\tilde{g}_{ij}^2 + \tilde{g}_{ji}^2) - \frac{1}{3}\delta_{ij}\tilde{g}_{kk}^2 \tag{9}$$

where δ_{ij} is the Kronecker delta and $g_{ij} = \partial u_i / \partial x_j$.

The convective flux is evaluated by a bounded central-differencing scheme that blends 98% of the 2nd-order central differencing scheme and 2% of the first-order upwind scheme for robustness purposes. The implicit unsteady solver with 2nd-order Euler implicit scheme is used to approximate the transient term. The physical time step (Δt) is set to 1.44×10^{-4} s, which ensures that the CFL (Courant Friedrichs Lewy) number lower than 1 in over 99% cells. LES simulation starts from the preliminary flow field that is provided by a URANS simulation with $k - \omega$ SST turbulence model. After a characteristic time ($t^* = tU_\infty / h$) of 65 when all the aerodynamic forces become dynamically stable, the LES simulation begins sampling and averaging results for a t^* of 129.

Fig. 5 shows the computational domain with a cross-sectional area of $6.5W \times 5W$, which accounts for a blockage ratio of about 2.4%. The length of the domain is $28W$ with $8W$ from inlet to bow tip-point and $16W$ from stern to outlet. The ship model sits on the floor with no gap in between. The coordinates system and velocity direction are denoted by x and u in the streamwise direction, y and v in the lateral (spanwise)

Table 2
Results of the grid independent study.

Cases	Max y^+	Max Δs^+	Max Δl^+	No. of cells	C_d	ΔC_d	C_y	ΔC_y
Initial	< 1	< 55	< 21	3.7 × 10^7	0.722	–	0.579	
Coarse	< 1	< 65	< 30	2.6 × 10^7	0.718	−0.55%	0.577	−0.35%
Refined	< 1	< 40	< 15	4.7 × 10^7	0.720	−0.28%	0.578	−0.17%

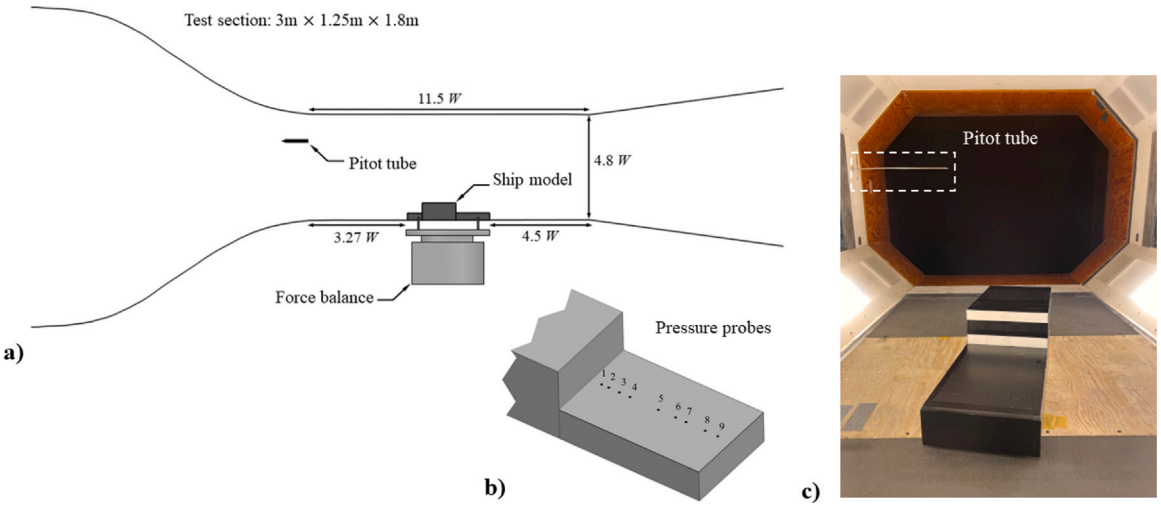

Fig. 4. Illustrations of the experimental setup: (a) schematics of Chalmers L2 wind tunnel, (b) locations of pressure probes on deck, (c) the Chalmers ship model placed in L2 wind tunnel with 10° yaw angle.

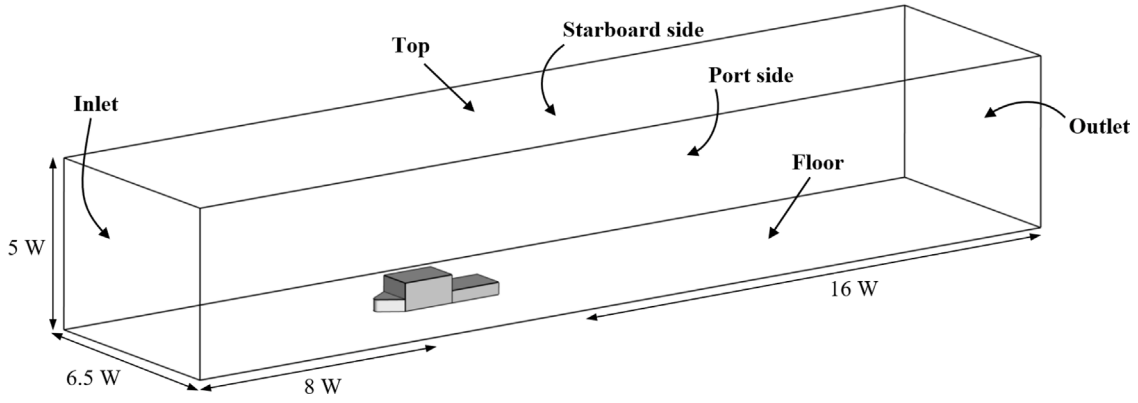

Fig. 5. Computational domain.

direction, and z and w in the vertical direction. As shown in Fig. 6, the free-stream u_∞ is added with a lateral component v_∞ to produce a 10° port-side wind U_p. The velocity inflow boundary condition with a uniform velocity U_p is specified at the inlet and port side of the computational domain shown in Fig. 5. Static pressure outlet boundary condition is applied at the outlet and the starboard side. The present setup of the inlet and outlet boundary conditions are adopted from the previous yaw-effect study on ships (Zhang et al., 2021). The top of the domain is specified with a symmetry boundary condition. The no-slip wall boundary condition is applied on the floor and all ship surfaces. For the cases with flow control, the velocity inlet boundary condition is specified at the injection exit without the injection duct simulated.

The structured hexahedral mesh is created using Pointwise. Fig. 7 shows the details of the mesh topology. The overall mesh size contains 37 million cells for the baseline model and 42 million cells for the model with flow control. The near-wall grid distance Δy is 3×10^{-5}, which ensures $y^+ = \frac{\Delta y u_\tau}{\nu}$ lower than 1. For the resolution in streamwise ($\Delta s^+ = \frac{\Delta s u_\tau}{\nu}$) and spanwise ($\Delta l^+ = \frac{\Delta l u_\tau}{\nu}$) directions, Δs^+ is less than 55 and the maximum Δl^+ is 21, which satisfies the suggested ranges

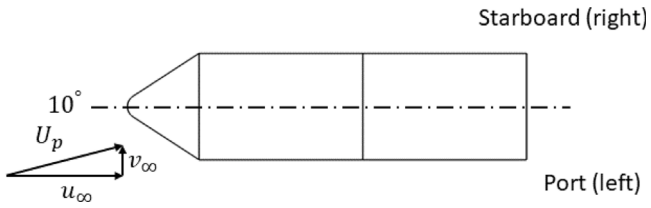

Fig. 6. 2D sketch of port-side free-stream U_p.

proposed by Piomelli and Chasnov (1996). Furthermore, as shown in Table 2, a grid dependency study is conducted based on a coarse mesh of 27 million cells and a refined mesh of 47 million cells. The acquired drag coefficients (C_d) and side force coefficients (C_y) fall in a very close range with those acquired from the initial mesh of 37 million cells. The deviation of ΔC_d is less than 0.6%, and ΔC_y is less than 0.3%. It also shows that both C_d and C_y acquired by the initial mesh are more

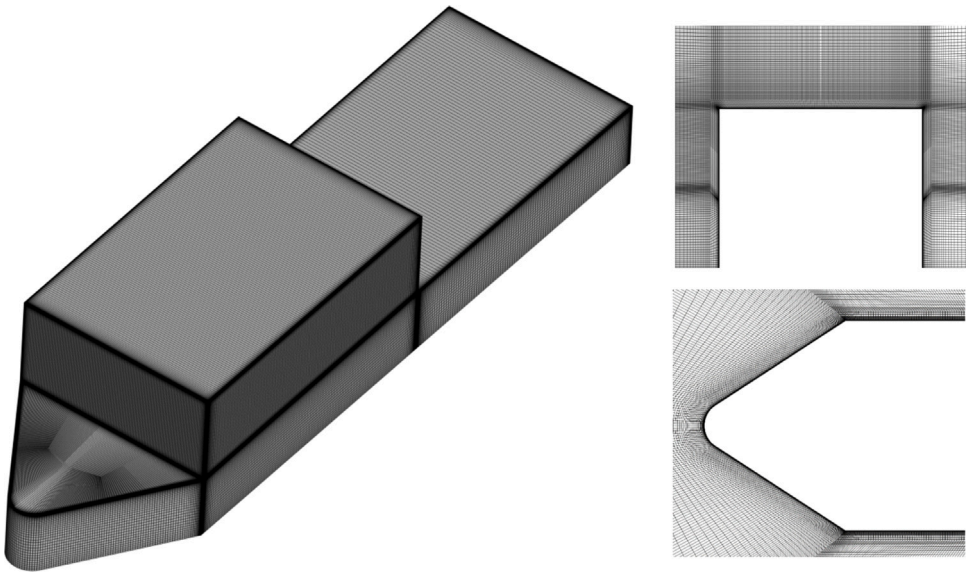

Fig. 7. Mesh topology of the Chalmers ship model (Xu et al., 2022).

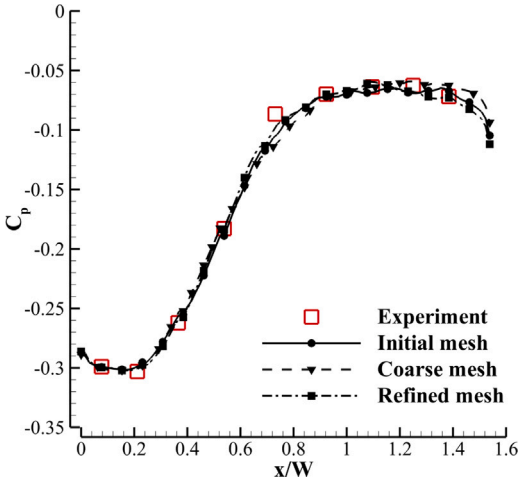

Fig. 8. The time-averaged C_p distribution at the center of deck.

consistence with the refined mesh, which suggests the convergence of solutions to the refined mesh. Note that the predicted drag and side forces are acquired by integrating the surface pressure and wall shear stress in x and y directions, respectively.

3. Results and discussions

3.1. Baseline validation

The numerical method is validated by comparing the C_d, C_y, and C_p distributions with the experimental measurements conducted under 10° yaw effect.

Table 3 compares the predicted C_d and C_y with the measured ones, where ΔC_d and ΔC_y indicate the deviations from the experiment. The drag coefficient C_d is 4.1% deviated from the experiment, and the side force coefficient C_y is 1.53% off.

Then, the C_p distribution along the center of the deck (Fig. 4(b)) is used for further validation. Fig. 8 shows that the predicted and measured C_p distributions are in a good agreement from base (x/W = 0) to deck-end (x/W = 1.54). Fig. 8 also shows that the predicted C_p distributions acquired by the three meshes virtually overlap with just

Table 3
Predicted and measured C_d and C_y.

Cases	C_d	ΔC_d	C_y	ΔC_y
Experiment	0.753	–	0.588	–
CFD	0.722	−4.10%	0.579	−1.53%

a slightly higher deviation observed in the coarse mesh at x/W from 1.2 to 1.6. Overall, it is indicated that the current numerical method is capable of predicting the flow around the CSM with satisfactory accuracy, and the grid independence is achieved with the initial mesh size of 37 million cells.

3.2. Numerical results of the baseline and flow control cases

This section presents the results of the controlled ship airflow under 10° yaw. Three cases are compared here, labeled as Cases 1–3: the baseline ship with square-back base, the modified ship base with roof and sides Coanda surfaces but no jet blowing, and the active flow control (AFC) case with jet blowing from both roof and two-sides slots. The AFC Case 3 has the total momentum coefficient C_μ of 0.02 with 0.0125 from the roof slot and 0.0075 from the side-slots.

The momentum coefficient C_μ is defined as

$$C_\mu = \frac{\dot{m}_j U_j}{0.5\rho_\infty {u_\infty}^2 A_s} \tag{10}$$

where $\dot{m}_j$ and U_j are the mass flow rate and velocity of the jet, respectively.

The flow structures of the three cases in the vicinity of the deck are illustrated in Fig. 9 using the 3D streamlines extracted from the time-averaged flow fields colored by the time-averaged u with the distribution of vortex cores marked by white lines. The 2D surface streamlines at the z-plane on the mid-hanger-height are also shown in the last column in Fig. 9. The pressure distribution at the base is colored by the time-averaged gauge pressure with a unit of [Pa]. Under the 10° port wind, significant yaw effects are manifested in the flow fields on deck. As shown in Fig. 9 (a), a re-circulation region with a z-direction vortex (ZV) can be observed at the starboard side downstream the base, which is substantially different from the horseshoe vortex structure (Shafer and Ghee, 2005) observed in zero-yaw cases. Such a ZV is caused by re-circulating the flow from starboard and hence, the base pressure is reduced due to the low-pressure vortex core. The

starboard flow also travels across the deck, however, blocked by the high-speed port-side flow and recirculates backwards and downstream as shown in Fig. 9 (b). Consequently, a low-speed region demonstrated by the iso-surface of $u = 0$ m/s and a port-side vortex (PV) are induced. With the sharp edges of the base rounded to Coanda surfaces in Case 2, leeward flow attaches on the starboard base as shown in Fig. 9 (d), (e), and (f). As a result, the low-speed region (iso-surface of $u = 0$ m/s) is suppressed and the z-direction vortex (ZV) observed in Case 1 is replaced by a streamwise vortex (SV) observed at the top-starboard corner of the base that is caused by the leeward flow interacting with the flow passing the roof Coanda surface. The SV has its core bounded on the base, which further reduces the base pressure. Similar to Case 1, the starboard flow in Case 2 travels across the deck but is blocked by the port-side flow, which also forms the port-side vortex (PV). With a C_μ of 0.02 applied in Case 3, the leeward flow and roof flow are energized at the near base region, which enhances the streamwise vortex in its core length and moves the vortex core towards the port. The low-speed region is further suppressed compared to Cases 1 and 2, which leads to the disappearance of the port-side vortex (PV). Due to the jet blowing, jet flow accelerates on the Coanda surfaces and reduces the surface pressure as can be observed on the sides and roof Coanda surfaces in Fig. 9(g) and (h).

Fig. 10 shows the instantaneous streamwise velocity (u_{ins}) at the symmetric and mid-deck-height planes. The suppression of the low-speed region downstream the base due to jet blowing is confirmed by the instantaneous contours where the low-speed region is constrained closer to the deck (Fig. 10(c)) as well as more to the port-side (Fig. 10(f)).

Fig. 11 shows the time-averaged u contours with the 2D streamlines at the symmetric plane. Three flow re-circulation regions are observed, one in the front of ship due to the blockage of superstructure, one near the leading edge of the roof due to the flow separating from the sharp edge, and the last one in the downstream of the base that is well discussed previously.

Fig. 12 shows the low-pressure region using the iso-surfaces of gauge static pressure at −5 and −4 (Pa), together with the white lines that mark the positions of vortex cores. A bulk of low-pressure region is observed downstream of the base due to the z-direction vortex (ZV). The port-side vortex (PV) also causes a low-pressure region near the port. Case 2 shown in Fig. 12(b) has the low-pressure region start to grow in the streamwise direction along the streamwise vortex core (SV). As the streamwise vortex is enhanced by the steady Coanda effect in Case 3, the low-pressure region is more stretched with its distribution presenting a pronounced streamwise pattern.

To evaluate the potential influence of the steady Coanda effect on the ship's stability and maneuverability. The coefficient of side forces (C_y) and yaw moments (M_y) of the three cases are compared in Table 4. Values of ΔC_y and ΔM_y are the reductions of the averaged side force and yaw moment compared to the baseline Case 1. The reductions of the RMS (root-mean-square) of side force (C_y) and yaw moment (M_y) are indicated by $\Delta\langle C_y\rangle$ and $\Delta\langle M_y\rangle$, respectively. The overall reduction of side force (ΔC_y) is broken down to the contributions from different parts of the ship model: port-side surface (ΔC_{yp}), starboard-side surface (ΔC_{ys}), and the rest (ΔC_{yr}, including jet effects and forces on the surfaces of roof, deck, base, bow, and stern). The yaw moment is the z-direction moment calculated by multiplying the side force with the x distance to a pivot fixing at the ship bow-tip point. As presented in Table 4, the 10° port-wind can generate significant side force and yaw moment for all cases, among which Case 1 has the highest values. With the steady Coanda effect applied in Case 3, the C_y and M_y are reduced by 5.27% and 7.97%, respectively. Table 4 also shows that the major changes of side force come from the side parts with the reduced side force on the windward port side and enhanced on the leeward starboard side as shown by the values of ΔC_{yp} and ΔC_{ys}.

To explain the cause of side force variations, Figs. 13 and 14 show the time-averaged static pressure (p_s) contours at starboard and port sides of the ship model. On the starboard side as shown in Fig. 13, a similar pressure distribution is observed on the major part of the surface with the only difference occurring at the side-Coanda surface, which is due to pressure reduction from the Coanda effect and streamwise vortices as demonstrated in Figs. 9 and 12. Such surface-pressure reduction contributes to the increased starboard side force of ΔC_{ys}. On the port, the pressure reduction is not only observed on the side-Coanda surface but also occupies more area in the upstream and downstream (enclosed by the dashed lines in Fig. 14(b) and (c)), which is the reason of the reduced ΔC_{yp}. For further explanation, Fig. 15 plots the u profiles perpendicular to the port-side surface at the three interested stations marked in Fig. 14. The D/W in Fig. 15 is the normalized distance from surfaces. It is observed that the near-surface velocity in all stations is increased in Cases 2 and 3 as compared to Case 1, which increases the dynamic pressure and therefore achieves the reduced static pressure on the port-side surface. Furthermore, Fig. 15 shows that the velocity increment is gradually enhanced as the flow approaches the side-Coanda surface, and the highest increment is achieved by Case 3 with jet blowing. This suggests an explanation for the increased near-surface velocity that the low pressure region in the vicinity of the side-Coanda surface appears to create a suction effect, which induces the upstream flow, leading to the velocity increment. The downstream static pressure is also affected as the upstream flow with increased velocity reaches the downstream. Overall, both sides of the ship model has pressure decreased with flow control applied; nevertheless the port side (windward) has a more enhanced pressure reduction, which results in the mitigation of the overall side force.

One of the important mean quantities is the streamwise velocity u on the ship deck. A higher incoming u velocity enables a helicopter takes off at a higher gross weight (Shafer and Ghee, 2005). Fig. 16 shows the time-averaged u contours at the three interested stations of $x/W = 0.2$, 0.8, and 1.35, where W is the width of deck, and $x/W = 0$ means the location of the hanger base. A low-speed region is observed at Station 1 in all cases, among which Case 3 with jet flow activated, have a significantly reduced size. The low-speed regions are reduced at both the port and starboard sides but has less reduction at port due to the re-circulation created by the cross-deck flow meeting with port main-flow as addressed previously with Fig. 9(b), (e), and (h).

During the recovery (landing) of a maritime helicopter, the turbulent fluctuation is one of the key factors that increases pilots' workload. The concerned region of turbulent fluctuation will depend on the selected recovery procedure. Here, we confine our interest to the Royal Navy's standard port-side forward-facing recovery (Roper et al., 2006), which is one of the most common routines. During the recovery as shown in Fig. 17, the helicopter approaches the deck hovering along the port-side deck and then performs a sidestep landing crossing the port-deck edge. In this regard, the turbulent fluctuation along the port-side deck plays a critical role in recovery efficiency.

To demonstrate the influence of the current AFC on the turbulent fluctuations at the concerned region, the turbulent kinetic energy (TKE), defined as $0.5(\overline{u'u'} + \overline{v'v'} + \overline{w'w'})$ is used here for discussion. Note that TKE is normalized by the square of the free-stream velocity ($u_\infty{}^2$). Fig. 18 shows the contours of TKE at three streamwise stations with the front view of Station 2 (mid-deck) for a better comparison. The starboard TKE at close-base Station 1 is increased in Case 3 but is quickly dissipated in the downstream Stations 2 and 3. As addressed previously, the port-side TKE is of more interest in helicopter recovery. It can be observed that the port-side TKE is suppressed in Case 3 for all stations. This is especially clear as demonstrated by the front views in the second row of Fig. 18. The high TKE region at the port side of Case 3 is smaller compared to the rest cases. Furthermore, Fig. 19 shows the high-shear-stress region along the port side using the iso-surface at $\overline{u'v'} = 0.03$ (normalized by $u_\infty{}^2$). Again, Case 3 achieves a largely mitigated shear-stress region as compared to Cases 1 and 2. The reduced TKE and $\overline{u'v'}$ will benefit a helicopter recovery under the yaw effect.

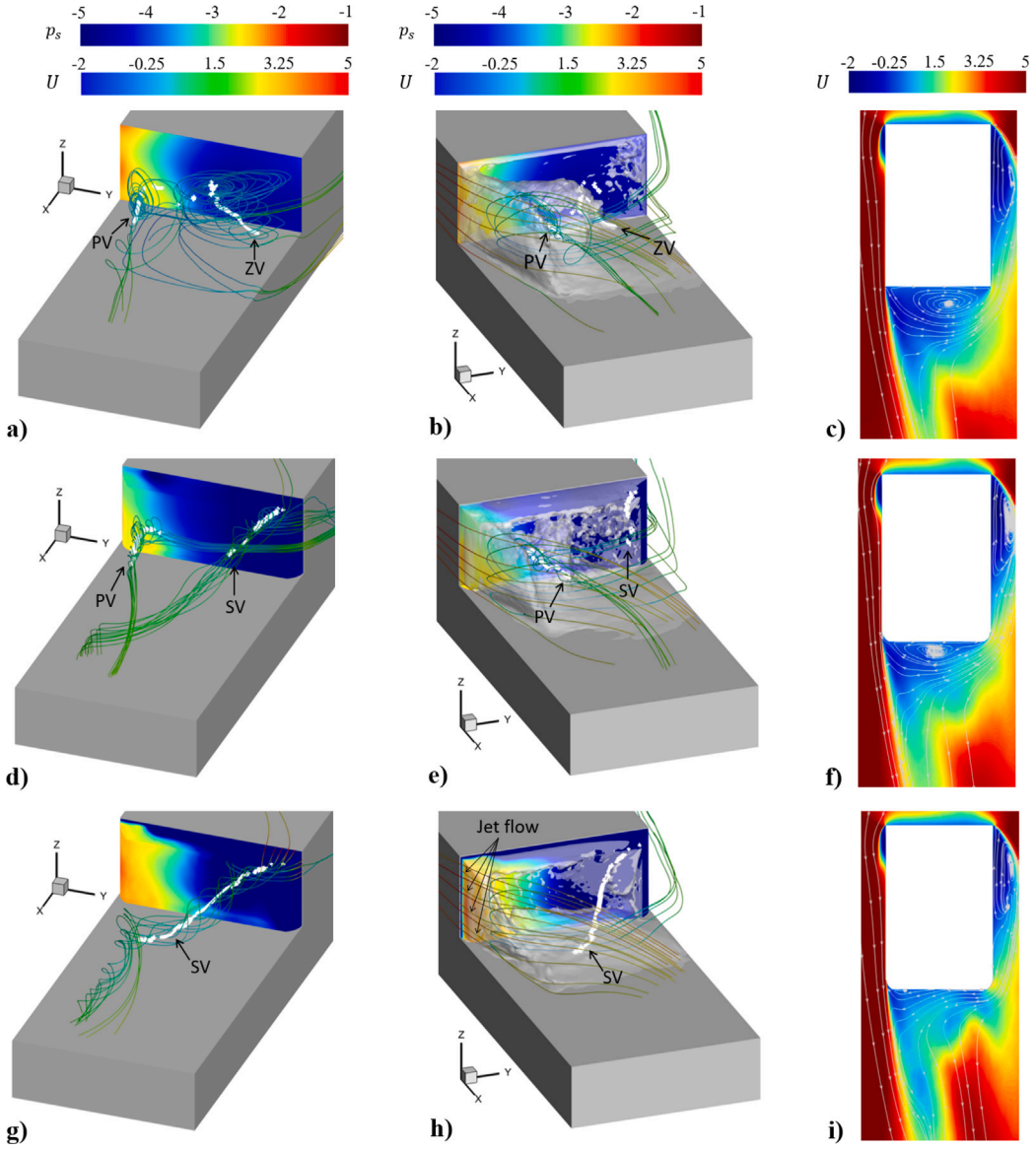

Fig. 9. The time-averaged static pressure distributions at the base and flow structures of the three cases: (a) (b) (c) Case 1, (d) (e) (f) Case 2, (g) (h) (i) Case 3; Column a-d-g is the starboard view showing the vortex cores and 3D streamlines colored by the time-averaged u; Column b-e-h is the port view showing cross deck flows and low speed zone of iso-surface with $u = 0$; Column c-f-i is the top view of 2D streamlines and the time-averaged u contours.

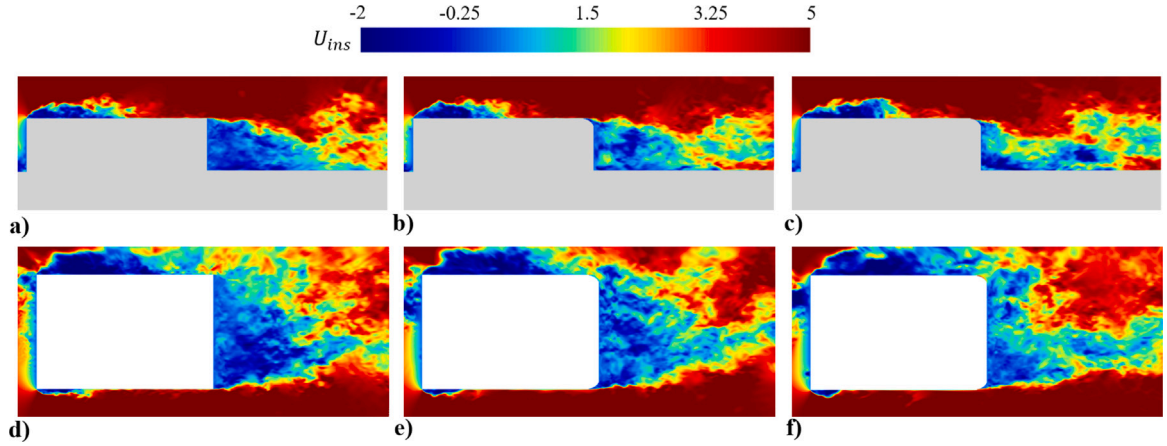

Fig. 10. The instantaneous streamwise velocity (u_{ins}) contours at the symmetric ($y = 0$) and mid-deck-height (z) planes: (a) (d) Case 1, (b) (e) Case 2, (c) (f) Case 3; Row a-b-c shows the contours at plane $y = 0$; Row d-e-f shows the contours at mid-deck-height z plane.

Table 4
Comparisons of the time-averaged side force coefficients and yaw moments.

Cases	C_y	M_y	ΔC_{yp}	ΔC_{ys}	ΔC_{yr}	ΔC_y	ΔM_y	$\Delta\langle C_y\rangle$	$\Delta\langle M_y\rangle$
Case 1	0.588	0.138	–	–	–	–	–	–	–
Case 2	0.567	0.130	−8.24%	4.61%	0.06%	−3.57%	−5.80%	−3.20%	−5.58%
Case 3	0.557	0.127	−11.68%	6.22%	0.19%	−5.27%	−7.97%	−4.95%	−7.46%

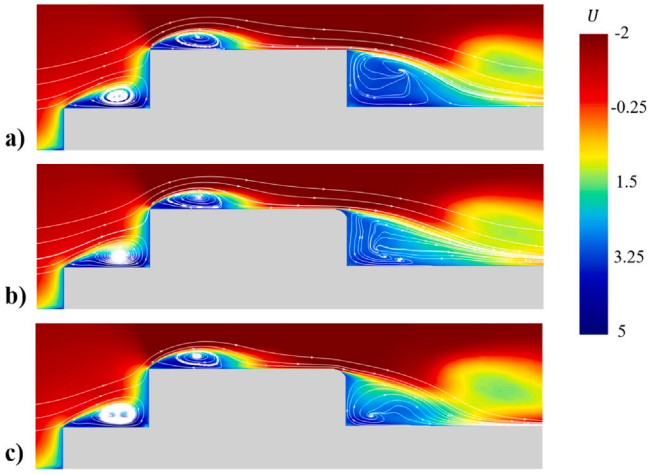

Fig. 11. The time-averaged u contours with 2D streamlines at the symmetric plane: (a) Case 1, (b) Case 2, (c) Case 3.

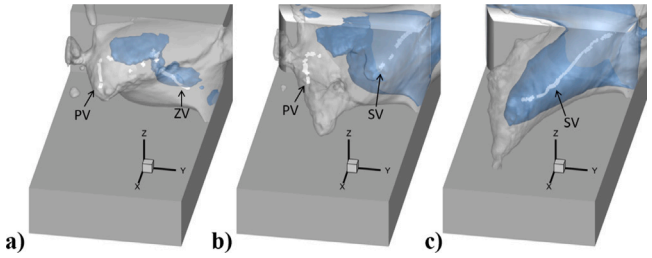

Fig. 12. Iso-surface of the time-averaged static pressure at $p_s = -5$ Pa (blue) and −4 Pa (gray) with vortex cores marked by white lines: (a) Case 1, (b) Case 2, (c) Case 3.

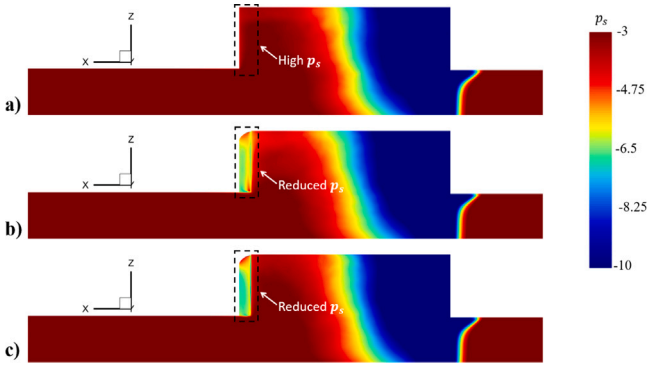

Fig. 13. The time-averaged static pressure contours at the starboard side (leeward) of CSM: (a) Case 1, (b) Case 2, (c) Case 3.

A question of interest is why the port-side TKE and $\overline{u'v'}$ are suppressed by the current active flow control. For a detailed discussion, Fig. 20 plots the time-averaged u, TKE, $\overline{u'v'}$, and the gradient of u ($\partial u/\partial y$) in the y (lateral) direction. These values are extracted from the three cases along the black dashed-dot lines in Station 2 (bottom row of Fig. 18), which cross the port-side high TKE region. Note that the data of $\partial u/\partial y$ is post-processed by a Gaussian-weighted moving average filter

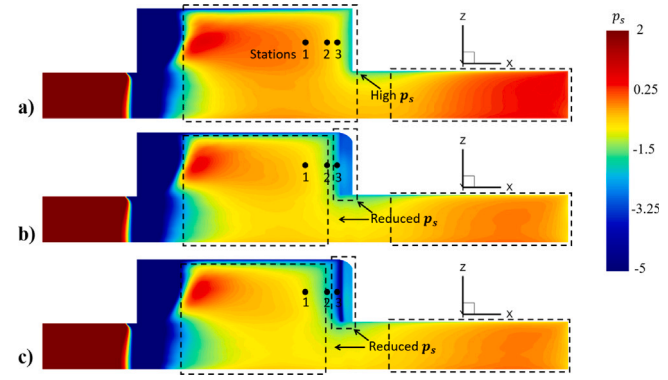

Fig. 14. The time-averaged static pressure contours at the port side (windward) of CSM: (a) Case 1, (b) Case 2, (c) Case 3.

using Matlab for more clear demonstration. As shown in the bottom of Fig. 20, the TKE of all three cases varies in the same pattern as their shear stresses $\overline{u'v'}$. The $\overline{u'v'}$ first increases towards $y/W = -0.4$ followed by a reduction towards $y/W = -0.2$, and so does TKE. This suggests that the TKE variation results from the shear stress variation, and the reduction in $\overline{u'v'}$ leads to the suppression of TKE. Now, the question becomes why the port-side $\overline{u'v'}$ is reduced in Case 3. The shear stress or the value of $\overline{u'v'}$ indicates there is a u velocity gradient along the y direction, and the larger the velocity gradient (in magnitude), the higher the $\overline{u'v'}$, which are supported by the fact observed in Fig. 19 that high-shear-stress regions are located at the boundary between high and low speed regions. For the current case, the port-side $\overline{u'v'}$ is caused by the low-speed cross-deck flow from starboard meeting with the high-speed port-side flow as demonstrated in Fig. 9(b), (e), and (h). With the AFC applied, the side-jet injected from the port-side slot in Case 3 not only suppresses low-speed region as shown in Figs. 16 and 19 but also serves as a buffer between the high and low speed flows as shown in Fig. 9(h), which all contribute to alleviating the velocity gradient. The alleviated velocity gradient can be observed in the $\partial u/\partial y$ plot in Fig. 20, where Case 3 maintains the lowest magnitude of velocity gradient before the $\overline{u'v'}$ and TKE reaches the maximum at $y/W = -0.4$. The u distribution shown on the top of Fig. 20 also demonstrates that the velocity of Case 3 drops in the mildest manner. Therefore, it is the alleviated velocity gradient achieved by the current AFC that suppresses $\overline{u'v'}$ and TKE. Compared to the baseline Case 1, the maximum TKE and $\overline{u'v'}$ in Case 3 are reduced by 15.0% and 37.2%, respectively.

4. Applying the current AFC on a real ship

For the future application of the current AFC on a real ship, three issues are considered and discussed in this section. The first issue is the Reynolds number effect. The Re for a real ship will be much higher than the model's, but the flow structures will be similar. This is because the bluff bodies (including the ship model) can achieve the independence of Re when it is higher than 2×10^4 (Sohankar, 2006; Lim et al., 2007), and the current study uses a Re of 8×10^4. Therefore, the effect of Re will not significantly affect the flow control results, and the conclusions acquired from the model should be the same as they are for a real ship.

The second issue is the implementation of the current AFC on a real ship. Apart from the base shape modifications (jet slots and Coanda surfaces) mentioned in the current paper, there are two more

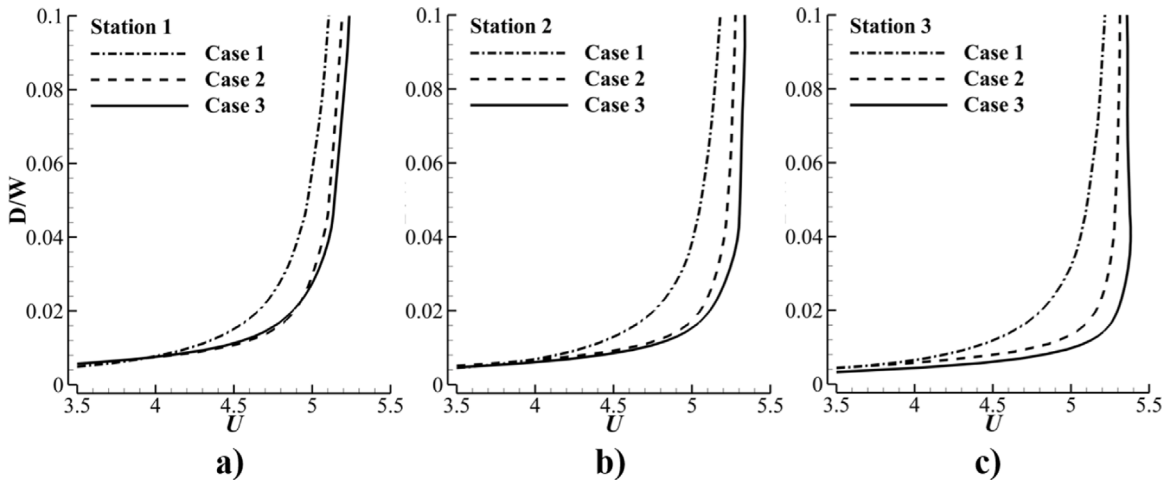

Fig. 15. The time-averaged u velocity profiles perpendicular to the port-side surface at: (a) Station 1, (b) Station 2, (c) Station 3; Location of stations is shown in Fig. 14.

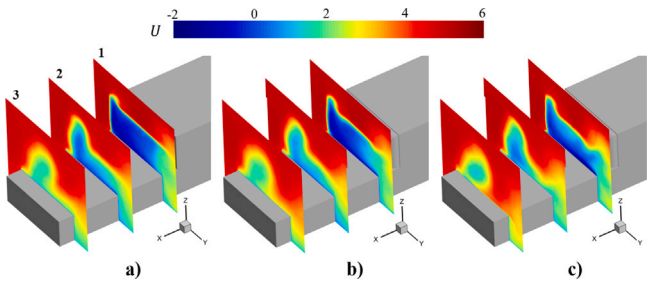

Fig. 16. The time-averaged u contours at different streamwise locations on deck: (a) Case 1, (b) Case 2, (c) Case 3.

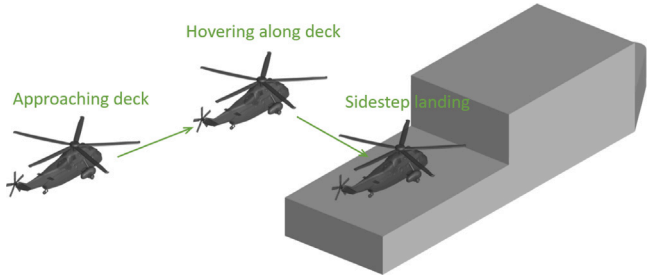

Fig. 17. Sketch of the helicopter recovery procedure, demonstrated using the Chalmers ship model.

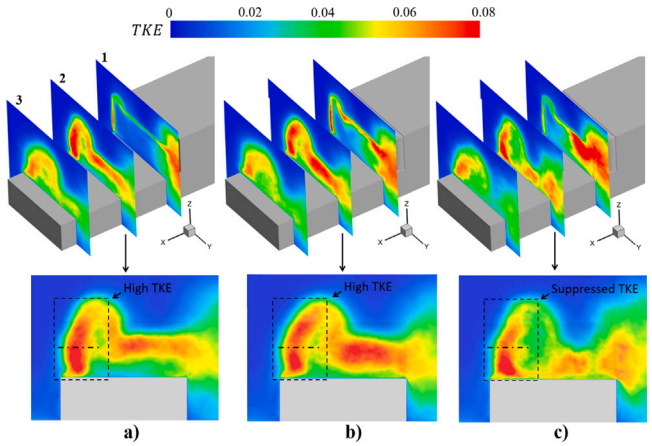

Fig. 18. Turbulent kinetic energy (TKE) contours at different streamwise locations on deck: (a) Case 1, (b) Case 2, (c) Case 3.

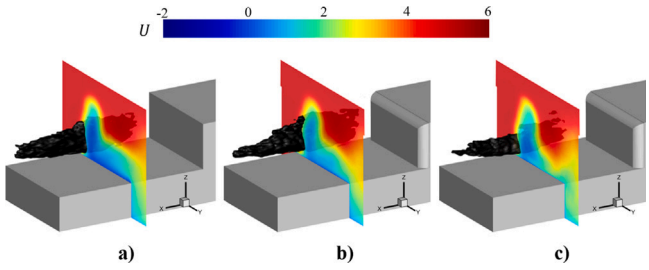

Fig. 19. The time-averaged u at Station 2 and iso-surface (black) of shear stress with $\overline{u'v'} = 0.03$: (a) Case 1, (b) Case 2, (c) Case 3.

modifications that need to be made. The first one is to have a flow source as the AFC jet supply. This can be achieved by using a pressure tank or redirecting pressurized high-energy flow from the compressor of the ship's gas turbine engine. The second modification is to design a pipe or ducting system that connects flow sources to the injection slot with the minimum frictional loss.

The third one is to determine the proper slot size and C_μ for a real ship. The injection slot size used here is normalized by the hanger height. When implementing the current AFC to a real ship, the actual slot size can be derived based on the real ship's hanger height. For the proper C_μ to be effective, it can be achieved by constantly adjusting the C_μ according to sailing environments and required control targets. Such control flexibility is also the major advantage of the current AFC method.

5. Conclusions

The present work studies the steady Coanda effect active flow control (AFC) for side force reduction and airwake manipulations under the yaw effect. The study is conducted numerically on the Chalmers ship model (CSM) using Large Eddy Simulation (LES) with Wall-Adapting Local-Eddy Viscosity (WALE) model. The AFC ship model is created by modifying the square-shaped hanger base to the Coanda surface with the addition of injection slots along the base's roof edge and two side edges. Three representative cases are studied for comparison: a baseline case, a no-jet case with the base modified to the Coanda surface, and an AFC case with jet blowing at a momentum coefficient (C_μ) of 0.02.

The results show that the base-shape modification significantly alters the vortex structure on deck from z-direction vortex (ZV) to streamwise vortex (SV), and the steady Coanda effect further enhances the SV with the removal of the port-side vortex (PV). As a result, the

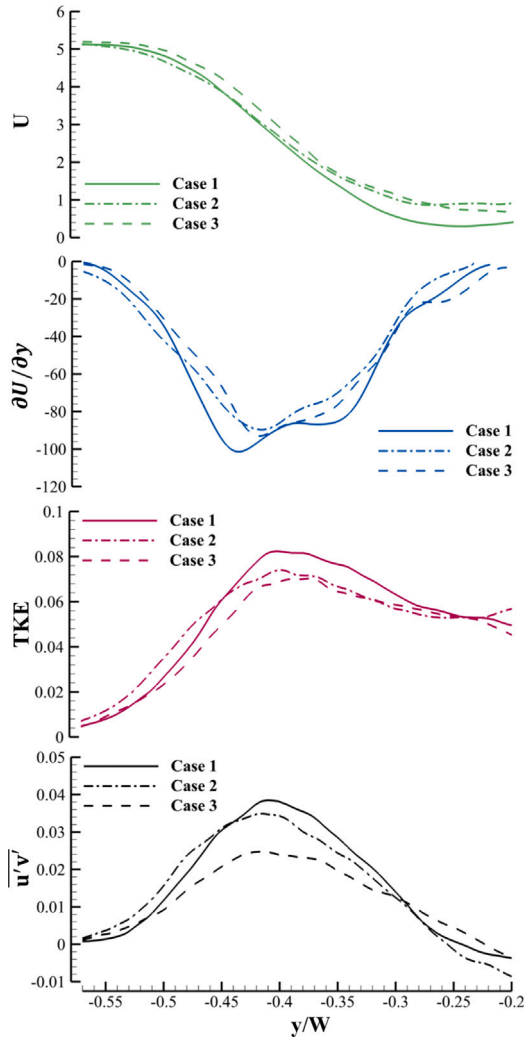

Fig. 20. Plots of the time-averaged u, $\partial u/\partial y$, TKE, and $\overline{u'v'}$ along y direction.

low-pressure region downstream of the base in the AFC case is more stretched with its distribution presenting a pronounced streamwise pattern. Due to the steady Coanda effect, the side force and yaw moment are mitigated by 5.27% and 7.97%, respectively, which can be attributed to the reduction of port-side (windward) surface static pressure. The steady Coanda effect can energize the flow on deck and reduce the areas of the low-speed region, especially on the starboard side. It is also found that the high-TKE (turbulent kinetic energy) region and high-shear-stress region along the port-side deck are significantly suppressed. Compared to the baseline case, the maximum TKE and $\overline{u'v'}$ in the AFC case are reduced by 15.0% and 37.2%, respectively. This is because the jet blowing from the side slot serves as a buffer between the high-velocity main flow at the port and the low-velocity recirculating flow, which alleviates the velocity gradient and thus mitigates the shear layer and TKE.

The present work, for the first time, studies the performance of the steady Coanda effect AFC on a ship model at yaw. It is demonstrated that the current AFC works well with the selected yaw angle and significant advantages are achieved including drag and side-force reduction, streamwise velocity recovery in the near wake, and TKE and shear layer suppression, which are beneficial to the ship's maneuverability and maritime helicopter operations. For future study, the focus is expected to be on the larger and various yaw angles for evaluating the performance of the current AFC in more comprehensive wind conditions.

CRediT authorship contribution statement

Kewei Xu: Conceptualization, Methodology, Software, Validation, Formal analysis, Investigation, Data Curation, Writing – original draft, Writing – review & editing, Visualization. **Xinchao Su:** Software, Investigation. **Yutao Xia:** Investigation. **Yitong Wu:** Investigation. **Rickard Bensow:** Validation, Writing – review & editing, Supervision, Project administration, Funding acquisition. **Sinisa Krajnovic:** Resources, Validation, Writing – review & editing, Supervision, Project administration, Funding acquisition.

Declaration of competing interest

The authors declare that they have no known competing financial interests or personal relationships that could have appeared to influence the work reported in this paper.

Data availability

Data will be made available on request.

Acknowledgments

This work is supported by the Chalmers University of Technology, Sweden. The authors would like to acknowledge the computing resource provided by SNIC (Swedish National Infrastructure for Computing) at the National Supercomputer Center (NSC) at Linköping University.

References

Aljure, D.E., Lehmkuhl, O., Rodriguez, I., Oliva, A., 2014. Flow and turbulent structures around simplified car models. Comput. & Fluids 96, 122–135.
Bardera, M.R., Matías García, J.C., García-Magariño, A., 2021. Aerodynamic optimization over frigate helicopter flight deck by hangar shape modifications. AIAA J. 59 (4), 1387–1397.
Bardera, R., Meseguer, J., 2015. Flow in the near air wake of a modified frigate. Proc. Inst. Mech. Eng. G 229 (6), 1003–1012.
Barros, D., Borée, J., Noack, B.R., Spohn, A., Ruiz, T., 2016. Bluff body drag manipulation using pulsed jets and Coanda effect. J. Fluid Mech. 805, 422–459.
Crozon, C., Steijl, R., Barakos, G.N., 2018. Coupled flight dynamics and CFD–demonstration for helicopters in shipborne environment. Aeronaut. J. 122 (1247), 42–82.
Dalla Longa, L., Evstafyeva, O., Morgans, A.S., 2019. Simulations of the bi-modal wake past three-dimensional blunt bluff bodies. J. Fluid Mech. 866, 791–809.
Findlay, D., Ghee, T., 2006. Experimental investigation of ship airwake flow control for a US Navy flight II-a class destroyer (DDG). In: 3rd AIAA Flow Control Conference. p. 3501.
Forrest, J.S., Owen, I., 2010. An investigation of ship airwakes using detached-eddy simulation. Comput. & Fluids 39 (4), 656–673.
Freund, J.B., Mungal, M.G., 1994. Drag and wake modification of axisymmetric bluff bodies using Coanda blowing. J. Aircr. 31 (3), 572–578.
Gallas, Q., Lamoureux, M., Monnier, J.-C., Gilliot, A., Verbeke, C., Delva, J., 2017. Experimental flow control on a simplified ship helideck. AIAA J. 55 (10), 3356–3370.
Geropp, D., Odenthal, H.-J., 2000. Drag reduction of motor vehicles by active flow control using the Coanda effect. Exp. Fluids 28 (1), 74–85.
Greenwell, D., Barrett, R., 2006. Inclined screens for control of ship air wakes. In: 3rd AIAA Flow Control Conference. p. 3502.
Haffner, Y., Borée, J., Spohn, A., Castelain, T., 2020. Unsteady Coanda effect and drag reduction for a turbulent wake. J. Fluid Mech. 899.
Herry, B.B., Keirsbulck, L., Labraga, L., Paquet, J.-B., 2011. Flow bistability downstream of three-dimensional double backward facing steps at zero-degree sideslip. J. Fluids Eng. 133 (5).
Jones, G.S., 2005. Pneumatic flap performance for a 2D circulation control airfoil, stedy & pulsed. Appl. Circ. Control Technol. 191–244.
Jones, G., Viken, S., Washburn, A., Jenkins, L., Cagle, C., 2002. An active flow circulation controlled flap concept for general aviation aircraft applications. In: 1st Flow Control Conference. p. 3157.
Kaaria, C., 2012. Investigating the Impact of Ship Superstructure Aerodynamics on Maritime Helicopter Operations (Ph.D. thesis). The University of Liverpool.
Kääriä, C.H., Wang, Y., White, M.D., Owen, I., 2013. An experimental technique for evaluating the aerodynamic impact of ship superstructures on helicopter operations. Ocean Eng. 61, 97–108.

Kee, J.-D., Kim, M.-S., Lee, B.-C., 2001. The COANDA flow control and Newtonian concept approach to achieve drag reduction of passenger vehicle. SAE Trans. 1383–1400.

LaSalle, N.R., 2013. Study of Passive Flow Control for Ship Air Wakes. Technical Report, NAVAL ACADEMY ANNAPOLIS MD.

Lim, H.C., Castro, I.P., Hoxey, R.P., 2007. Bluff bodies in deep turbulent boundary layers: Reynolds-number issues. J. Fluid Mech. 571, 97–118.

Nicoud, F., Ducros, F., 1999. Subgrid-scale stress modelling based on the square of the velocity gradient tensor. Flow Turbul. Combust. 62 (3), 183–200.

Nisham, A., Terziev, M., Tezdogan, T., Beard, T., Incecik, A., 2021. Prediction of the aerodynamic behaviour of a full-scale naval ship in head waves using detached eddy simulation. Ocean Eng. 222, 108583.

Piomelli, U., Chasnov, J.R., 1996. Large-eddy simulations: Theory and applications. In: Turbulence and Transition Modelling. Springer, pp. 269–336.

Rhoades, M.M., Healey, J.V., 1992. Flight deck aerodynamics of a nonaviation ship. J. Aircr. 29 (4), 619–626.

Roper, D.M., Owen, I., Padfield, G.D., Hodge, S.J., 2006. Integrating CFD and piloted simulation to quantify ship-helicopter operating limits. Aeronaut. J. 110 (1109), 419–428.

Seele, R., Graff, E., Lin, J., Wygnanski, I., 2013. Performance enhancement of a vertical tail model with sweeping jet actuators. In: 51st AIAA Aerospace Sciences Meeting Including the New Horizons Forum and Aerospace Exposition. p. 411.

Sellars, N., Wood, N., Kennaugh, A., 2002. Delta wing circulation control using the coanda effect. In: 1st Flow Control Conference. p. 3269.

Shafer, D., Ghee, T., 2005. Active and passive flow control over the flight deck of small naval vessels. In: 35th AIAA Fluid Dynamics Conference and Exhibit. p. 5265.

Shukla, S., Singh, S.N., Sinha, S.S., Vijayakumar, R., 2021. Comparative assessment of URANS, SAS and DES turbulence modeling in the predictions of massively separated ship airwake characteristics. Ocean Eng. 229, 108954.

Sohankar, A., 2006. Flow over a bluff body from moderate to high Reynolds numbers using large eddy simulation. Comput. & Fluids 35 (10), 1154–1168.

Syms, G.F., 2008. Simulation of simplified-frigate airwakes using a lattice-Boltzmann method. J. Wind Eng. Ind. Aerodyn. 96 (6–7), 1197–1206.

Tritton, D.J., 2012. Physical Fluid Dynamics. Springer Science & Business Media.

Xu, K., Su, X., Bensow, R., Krajnović, S., 2022. Drag reduction of ship airflow using steady Coanda effect. Ocean Eng. 266, http://dx.doi.org/10.1016/j.oceaneng.2022.113051.

Xu, K., Su, X., Bensow, R., Krajnovic, S., 2023. Large eddy simulation of ship airflow control with steady Coanda effect. Phys. Fluids 35, http://dx.doi.org/10.1063/5.0127560.

Yongjie, S.H.I., Xiang, H.E., Yi, X.U., Guohua, X.U., 2019. Numerical study on flow control of ship airwake and rotor airload during helicopter shipboard landing. Chin. J. Aeronaut. 32 (2), 324–336.

Zan, S.J., 2001. Surface flow topology for a simple frigate shape. Can. Aeronaut. Space J. 47 (1), 33–43.

Zhang, J., Minelli, G., Basara, B., Bensow, R., Krajnović, S., 2021. Yaw effect on bi-stable air-wakes of a generic ship using large eddy simulation. Ocean Eng. 219, 108164.